Guidelines for Volume Force Distributions Within Actuator Line Modeling of Wind Turbines on Large-Eddy Simulation-Type Grids

Pankaj K. Jha
Department of Aerospace Engineering,
The Pennsylvania State University,
University Park, PA 16802

Matthew J. Churchfield
Senior Engineer
National Wind Technology Center,
National Renewable Energy Laboratory,
Golden, CO 80401

Patrick J. Moriarty
Senior Engineer
National Wind Technology Center,
National Renewable Energy Laboratory,
Golden, CO 80401

Sven Schmitz
Assistant Professor
Department of Aerospace Engineering,
The Pennsylvania State University,
University Park, PA 16802

The objective of this work is to develop and test a set of general guidelines for choosing parameters to be used in the state-of-the-art actuator line method (ALM) for modeling wind turbine blades in computational fluid dynamics (CFD). The actuator line method is being increasingly used for the computation of wake interactions in large wind farms in which fully blade-resolving simulations are expensive and require complicated rotating meshes. The focus is on actuator line behavior using fairly isotropic grids of low aspect ratio typically used for large-eddy simulation (LES). Forces predicted along the actuator lines need to be projected onto the flow field as body forces, and this is commonly accomplished using a volumetric projection. In this study, particular attention is given to the spanwise distribution of the radius of this projection. A new method is proposed where the projection radius varies along the blade span following an elliptic distribution. The proposed guidelines for actuator line parameters are applied to the National Renewable Energy Laboratory's (NREL's) Phase VI rotor and the NREL 5-MW turbine. Results obtained are compared with available data and the blade-element code XTURB-PSU. It is found that the new criterion for the projection radius leads to improved prediction of blade tip loads for both blade designs. [DOI: 10.1115/1.4026252]

1 Introduction

1.1 Wind Turbines in the Atmosphere. Wind energy is currently one of the most readily available sources of renewable energy. Various reports [1–3] state that high penetrations of wind-driven electrical generation, 20% and greater of the electrical demand, are technically feasible. However, the wind industry faces a number of challenges today in developing wind farms, both land-based and offshore, some of which involve the aerodynamics within the wind farm. Wind turbine wakes interact with turbines located downstream, with other wakes, and with the turbulent atmospheric boundary layer (ABL). Although accurate wake modeling is necessary to accurately predict annual energy production of wind farms, a difficult challenge is to understand the details of how atmospheric turbulence and wakes affect both power production and transient mechanical loading at the turbine level. For example, the wind energy community is now well aware of the fact that the atmospheric stability state, which has a direct impact on the nature of the atmospheric turbulence, plays an integral role in the recovery of the wake momentum deficit downstream of a wind turbine, thus having a profound effect on the performance of a given wind turbine array or wind farm [4,5]. Also, experimental measurements show that differences in atmospheric turbulence at night versus day cause differences in mechanical loading [6]. At this time, fully blade-resolved simulations subject to resolved turbulent inflow are only possible with hybrid Reynolds-averaged Navier–Stokes (RANS)–LES, which is computationally expensive and precludes the simulation of an entire wind farm. It is here that the actuator turbine aerodynamics concept, in conjunction with CFD, offers the potential for accurately predicting unsteady wind turbine wakes at a feasible computational cost. This places actuator methods between low-fidelity engineering models [7–10] and fully blade-resolved CFD simulations. The reduced cost of actuator simulations as opposed to fully blade-resolved simulations enables the simulation of an entire wind farm immersed in an ABL flow consisting of hundreds of turbines and subject to resolved turbulent inflow using LES. Simulations of this type will help fill the knowledge gap concerning atmospheric turbulence–turbine interactions, a gap that when filled will allow for improved reduced-order wind turbine and wind farm design tools.

1.2 Actuator Modeling of Wind Turbines. The lowest-order actuator-type method to model wind turbines is the actuator disk method (ADM) that was first developed for RANS solvers by Sørensen et al. [11], Leclerc and Masson [12,13], Réthoré et al. [14], and Mikkelsen [15]. The actuator disk concept replaces the actual wind turbine rotor by a force disk that enters the momentum equations of the underlying flow solver. Details, such as the blade root and tip vortices and the blade boundary layer, are not modeled. However, the ADM accounts for large-scale unsteady interaction of the overall wake with the turbulent ABL flow. At present, several efforts are underway that use LES and the actuator disk concept to model large wind farms. Some examples are the works of Ivanell et al. [16], Meyers and Meneveau [17], Singer et al. [18], and Stovall et al. [19].

The next step in model fidelity is the ALM. ALMs model individual blade loads by a suitable distribution of body forces along the blade whose strengths are determined from sectional inflow conditions and blade-element type table lookup of airfoil properties. Details, such as root and tip vortices, are captured. Most of the current state-of-the-art ALMs are rooted in the work of Sørensen and Shen [20]. Further developments are followed by Troldborg [21], Troldborg et al. [22,23], and Sibuet Watters and

Contributed by the Solar Energy Division of ASME for publication in the JOURNAL OF SOLAR ENERGY ENGINEERING. Manuscript received April 25, 2013; final manuscript received December 5, 2013; published online January 10, 2014. Assoc. Editor: Yves Gagnon.

2013.04 ===2013.12==2014.01

投影力的目的是为了避免数值不稳定

Masson [24]. In order to prevent numerical instabilities and to transform the line force into a volumetric force, the body forces are projected throughout a finite volume surrounding the actuator line. Most commonly and for ease of implementation, the projection function has a Gaussian shape [11–15,20,22,23]. Some examples of the use of the ALM in conjunction with LES are the works of Lu and Porté-Agel [25] and Conzemius et al. [26]. Recently, the ALM of Sørensen and Shen [20] has been implemented into an ABL-LES solver created using the open-source field operation and manipulation (OPENFOAM) CFD toolbox [27] by researchers at the NREL [28,29]. The solver has demonstrated its potential to model large wind farms and overall wake effects [4,30].

ASM不仅考虑展向分布还可以考虑弦向分布

In the past few years, the ALM has been extended to actuator surface methods. In this method, each blade is represented as a surface corresponding to the planform of the blade. Not only can the radial distribution of force be specified, but also the chordwise distribution. Therefore, actuator surface methods do not, in principle, suffer from the same problematic issues associated with the volumetric force distribution as do ALMs. Some examples are the works of Dobrev et al. [31], Shen et al. [32], and Sibuet Watters and Masson [24] where the latter method has been successful in explicitly specifying pressure and velocity jumps at a rotating actuator surface element. However, actuator surface methods require finer grids associated with an increased computational cost compared with the ALM. This is one of the reasons why actuator surface methods are not used in state-of-the-art simulations of large wind farms.

1.3 Current Issues in the State-of-the-Art ALM. Though the ALM has advanced to become one of the most widely accepted computational methods for predicting the wakes of individual wind turbines and wake interactions in turbine arrays and larger wind farms, there is a need within the wind energy community for guidelines in choosing ALM parameters. The most important ALM parameters are (i) radius of the body-force projection function, ε, (ii) the grid spacing Δ_{grid} along the actuator line, and (iii) the spacing Δ_b between actuator points. Following Sørensen et al. [11], the projection function used in this study is a three-dimensional Gaussian, with equal width in all three coordinate directions. There is no consensus on the ideal Gaussian radius ε. One view is that the radius should be as small as possible to obtain a very compact representation of the force distribution along the actuator line, thus better approximating a line force. Another view is that the width should spread the force over a region similar to the actual force; on a real blade, the force is distributed over the blade radially and chordwise. The lower threshold for ε is, in general, governed by numerical stability. Troldborg [21] suggests that $\varepsilon/\Delta_{grid} = 2$ be chosen along the actuator line as a compromise between numerical stability and accurate prediction of turbine power. For a Gaussian radius constant along the blade span, the grid spacing Δ_{grid} is typically chosen such that there are between 30 and 60 grid points along the actuator line with a spacing Δ_b between actuator points complying with $\Delta_b \leq \Delta_{grid}$. Martínez et al. [33] have found that the turbine power predicted by the ALM is, indeed, very sensitive to the Gaussian radius ε. They found that at a given inflow wind speed and a given ε, the computed rotor power converges as the grid is refined; however, as $\varepsilon/\Delta_{grid}$ is varied from 2 to 10.5, the predicted power increases by about 25%, which is significant. It is also known that a constant Gaussian radius ε leads to blade tip loads being overpredicted [34]. To alleviate this problem, a tip-loss function, e.g., the Prandtl tip-loss factor [35] or the more advanced F1 correction suggested by Shen et al. [36–38], is often added to the ALM method when using a constant value of ε along the actuator line. Such ad hoc corrections have shown improved predictions of blade tip loads. Although very valuable in the current state of the practice, tip-loss corrections, in general, derive from classical blade-element momentum (BEM) methods that have no other means of including tip effects. In contrast, the ALM resolves the full three-dimensional flow field around the actuator line, however only as a first-order approximation of the true blade loading. It is therefore arguable whether an adjusted volumetric force distribution within the ALM in the tip region can be an alternative method of coping correctly with the blade tip loads. The recent work of Shives and Crawford [39] is a step ahead toward general requirements for the Gaussian radius ε and the grid spacing Δ_{grid}. Their hypothesis is that the Gaussian radius ε at a given spanwise station along the actuator line should be proportional to a representative physical dimension of the local blade section, such as the blade chord c, while remaining to be a multiple of the grid spacing Δ_{grid} to keep numerical stability. They modeled an elliptic wing with an aspect ratio of AR = 10.2 within a RANS solver and found that $\varepsilon/c = 0.25$ and $\varepsilon/\Delta_{grid} \geq 4$ lead to accurate prediction of the expected constant downwash. It is worth mentioning that their method does not require any tip-loss correction factor. Although the work of Shives and Crawford [39] is clearly an advancement of the state-of-the-art ALM, it requires about 100 grid points along the actuator line for an elliptic wing of AR = 10.2. For comparison, the notional design of the NREL 5-MW reference wind turbine [40] with AR ≈ 18 would require an even finer grid spacing along the actuator line, a requirement that is not computationally feasible when using the ALM method for LES simulations of large wind farms.

To date, no universal guidelines are available for ALM parameters to be used in LES simulations of wind turbine wakes that lead to consistent results among various rotor designs and grid resolutions. An attempt was made by Martínez et al. [33], but further work is necessary. As opposed to RANS computations, LES requires cell aspect ratios close to unity. This eliminates the possibility of large grid refinement in the axial direction around the actuator line as used, for example, in the works of Sibuet Watters and Masson [24] and Shives and Crawford [39] and poses an additional difficulty to the accuracy of computed blade loads in conjunction with rotor thrust and power. In LES, the required grid spacing is on the order of the blade chord with the intent to resolve turbulent eddies down to that scale and their interaction in the wake with larger-scale eddies advected by the ABL flow. In general, between 30 and 60 grid points along the actuator line is a desirable number in terms of the trade-off between resolution and computational cost for LES of conventional wind turbine blades.

1.4 Contributions of This Work. This work improves the predictive capability of the state-of-the-art ALM on LES-type grids and provides guidelines to obtain consistent results for different rotor designs and grid spacings. An integral part of the present effort is a rigorous study that quantifies the sensitivity of computed sectional blade loads as well as integrated rotor thrust and power on the major ALM parameters ε, Δ_{grid}, and Δ_b. All simulations are performed with steady and uniform inflow only. The paper is organized as follows: Section 2 gives a brief description of the ALM and its current implementation in an OPENFOAM-based LES solver. Next, a new method is presented in which the Gaussian radius ε is based on an equivalent elliptic blade planform of the same AR as the actual blade. The basic idea of the new method was inspired by the work of Schrenk [41] used in the fixed-wing community and leads to a set of universal criteria to be used for the ALM parameters on LES-type grids. In Sec. 3, available data for the NREL Phase VI rotor [42] and BEM results are used for quantitative comparisons against results obtained by ALM runs with various parameter settings. Comparisons between the currently used settings and the proposed new criteria are performed. It is found that the new method for the Gaussian radius ε and guidelines for the grid spacing Δ_{grid} and actuator spacing Δ_b yield improved and consistent predictions for sectional blade loads. Also, ALM simulations are performed for the NREL 5-MW turbine and compared with BEM results. It is again found that the new method in which the Gaussian radius ε is determined by an equivalent elliptic blade planform gives consistent and improved

激励线只是完全三维流场的一阶模态近似。

能否通过调整体积力的分配来正确处理梢部载荷呢？

网格：1
半径：4
弦长：16

基于弦长的分布不需要梢部损失修正。

LES要求各项同性网格，因此不能单独对网格在径向加密

AL有三个重要参数：
投影半径
网格间距
激励点距离

LES要求网格间距与弦长相当，来解析弦长及以上尺度湍流涡及其与尾流和ABL中对流结构的干扰。

叶片的激励点一般有30-60个点。
点的间距小于网格间距

Martinez发现Cp对半径敏感现象，试验了网格收敛，但变化很大

等效弦长

NASA的老文章

固定分配半径会导致梢部载荷过高，为此一般需要梢部损失修正。

predictions of sectional blade loads. The paper concludes with recommendations for users of the ALM on LES-type grids.

2 Numerical Methods

2.1 The ALM in the ABL-LES OPENFOAM Solver. The ALM within OPENFOAM is being actively developed and maintained by researchers at NREL and The Pennsylvania State University. The OPENFOAM CFD toolbox [27] is a set of C++ libraries meant for solving partial differential equations. The solver we use in this study is an unstructured, incompressible, finite-volume solver. We use second-order accurate spatial differencing with a small blend of upwinding, as is discussed later. Time integration is also second-order accurate using the Crank–Nicolson method. The solution is advanced using the pressure-implicit splitting operation (PISO) algorithm of Issa [43]. The set of linear equations resulting from the discretization of the momentum predictor is solved using an iterative preconditioned conjugate gradient method. The linear equations resulting from the discretization of the pressure equation are solved using an iterative multigrid method. Velocity–pressure decoupling is avoided by using the method of Rhie and Chow [44]. Because we are performing LES, a subgrid-scale model is necessary, and we use the standard Smagorinsky model [45] with a model constant of 0.168, the optimal value for isotropic turbulence.

空间离散格式为：具有很小的迎风性质的两阶中心差分格式

时间格式：2阶 C-N格式

动量方程：PCG

压力方程：多重网格法

rhie-chow插值避免速度-压力失耦

标准 Smagorinsky 模型，常数0.168

The default ALM is that of Sørensen and Shen [20], and the underlying LES solver is capable of modeling both uniform and ABL flow. The rotor blade is discretized by a finite number (typically 30–60) of actuator points. The lift and drag forces computed at these actuator points are projected onto the background Cartesian grid as body forces in the momentum equation. The last term in the momentum equation (1) corresponds to the body-force term

默认ACL方法是shen的方法，叶片一般是30-60网格

$$\frac{D\boldsymbol{u}}{Dt} = \mathrm{RHS} + \mathbf{F}_p \tag{1}$$

力源项的结果是：激励线周围存在压力跳跃。附着涡和尾涡

The effect of the body-force term in Eq. (1) is a pressure jump across the actuator line and the formation of bound and trailing vorticity. The projection from discrete actuator point blade loads $\mathbf{f}_{N,m}$, in which N represents the blade index and m denotes the actuator point index, to a volumetric body force $\mathbf{F}_p$ is typically achieved by a Gaussian function as shown in the following equation:

$$\mathbf{F}_p(x_p, y_p, z_p, t) = -\sum_N \sum_m \mathbf{f}_{N,m}(x_{N,m}, y_{N,m}, z_{N,m}, t)\eta_{N,m} \tag{2}$$

where

$$\eta_{N,m} = \frac{1}{\varepsilon^3 \pi^{3/2}} \exp\left[-\left(\frac{|\boldsymbol{r}|}{\varepsilon}\right)^2\right] \tag{3}$$

Here, $|\boldsymbol{r}|$ is the distance from grid cell p to the actuator point. A more detailed description of the solver has been presented in earlier work [4,28–30]. The ALM finds sectional lift and drag forces that define the force vector $\mathbf{f}_{N,m}$ by determining the local flow velocity and angle of attack (AOA) that is then applied to an airfoil lookup table. In this work, local velocity is sampled directly at the center of each actuator line element. Because the velocity is sampled at the center of each actuator element, which is the center of the bound vortex circulating about the actuator line, the effects of the upwash and downwash created by the bound vortex are not seen.

由于速度是在激励单元处采样得到，因此附着涡对该点的上洗和下洗可以忽略。

但尾流的诱导下洗角不能忽略。

The governing equations are solved using the finite-volume method on unstructured meshes. All variables are cell-centered and collocated on the grid. To avoid the pressure–velocity decoupling that occurs with collocated, incompressible solvers, the velocity fluxes at the finite-volume faces are constructed using an interpolation similar to that of Rhie and Chow [44]. All other interpolation from cell centers to faces is a mix of either linear (second-order central differencing) or midpoint (second-order central differencing with equal weighting regardless of mesh stretching, see Eq. (2.20) and pages 31–33 of Wesseling's [46] notes for a description) mixed with a very small amount of first-order upwinding.

因为OPenfoam中的同位网格处理与原始的rhi-chow插值有所区别

As the flow encounters the actuator line body-force field, some oscillations are observed in velocity and pressure emanating from the actuator line if pure linear or midpoint interpolation is used, which is shown in Fig. 1(*a*) in the flow past a stationary two-dimensional actuator line. Even using Troldborg's [21] rule of thumb in which $\varepsilon/\Delta_{\mathrm{grid}} = 2$, these oscillations occur. Troldborg, however, used a blend of 90% fourth-order central differencing and 10% third-order quadratic upwind interpolation for convective kinetics differencing. To remove these oscillations, we tried using a blend of 90% second-order linear/10% first-order upwind interpolation upstream of the actuator line and 98% linear/2% upwind everywhere else with a smooth transition in blending between these zones. This was successful in removing the oscillations, as can be seen in Fig. 1(*b*), while still preserving the wake structure. The same is observed for the rotating actuator lines of a modeled turbine rotor. Time advancement uses Issa's [43] PISO algorithm, which is an implicit predictor/corrector scheme. The implicit terms are integrated in time using second-order Crank–Nicolson discretization. We use one predictor followed by three correctors. The momentum transport equation is solved directly. However, to enforce the continuity equation, the divergence of the discrete momentum transport equation is taken, which results in an elliptic equation for the modified pressure. The momentum transport equations are solved using an iterative diagonal incomplete-lower-upper preconditioned biconjugate-gradient linear system solver. The pressure equation, which is the most expensive to solve, is solved using a geometric agglomerated algebraic multigrid solver. The code is parallelized using the message-passing interface. Figure 2 shows an example of instantaneous vorticity magnitude contours in an axial plane.

线性插值存在一定的数值震荡

一个动量预估+三个压力修正

ILU PBICG

GAMG

ALM simulations were performed on grids with several refinement zones within an outer baseline grid. The outer grid dimensions span from −5 D to +10 D in the streamwise and −5 D to +5 D in the other two directions with the turbine location as the reference point. The innermost refinement region extends from −1.5 D to +10 D in the streamwise and −1.25 D to +1.25 D in the other two directions. The domain sizes used are similar to those documented in the literature [22]. Depending on the grid resolution used in the innermost refinement zone around the actuator line, the total number of grid cells ranged between 16 and 24 million. The time steps used in the simulations are determined by a more stringent condition than the standard Courant–Friedrichs–Lewy (CFL) criterion. In all cases, the time step is chosen such that the blade tip does not traverse more than one grid cell per time step in the innermost refined zone close to the actuator line.

2.2 General Guidelines for ALM Parameters. As mentioned in Sec. 1, the main parameters that affect the volumetric

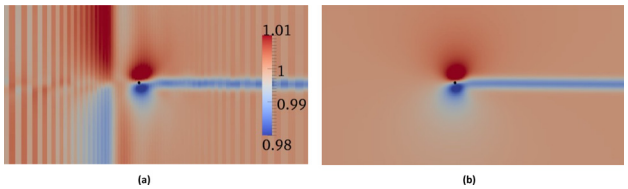

Fig. 1 A contour of the streamwise velocity normalized by freestream velocity taken in a plane perpendicular to the actuator line and at midspan using purely linear interpolation (*a*) or a spatially varying blend of midpoint and upwind interpolation (*b*). The point where the actuator line intersects these contours is shown with a black dot.

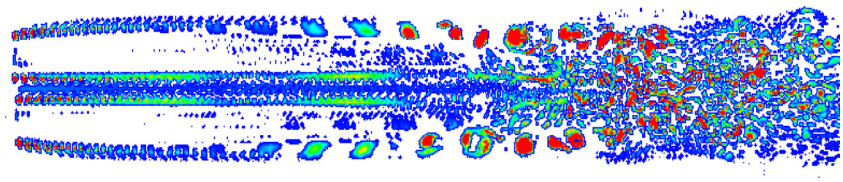

Fig. 2 Vorticity magnitude in an axial wake plane (NREL 5 MW wind turbine, $V_{Wind} = 8$ m/s). In this example, the wind turbine rotor is subject to uniform inflow conditions. Root and tip vortices as well as the expansion of the streamtube are clearly visible in the near wake. The wake flow becomes unstable approximately 1.5 rotor diameters downstream of the turbine, where the laminar shear layer transitions to turbulent flow. The breakdown of large turbulent eddies into smaller ones is visible further downstream.

梢涡大概在1.5D后破碎，层流剪切层转捩成湍流

三大重点参数

distribution of body forces $\mathbf{F}_p$ around the actuator line are the Gaussian radius ε, the grid spacing Δ_{grid} in the vicinity of the actuator line, and the distance between actuator points Δ_b. To date, the main lessons learned about the choice of ALM parameters are: i) that the Gaussian radius ε should be small, to resemble a line, but must be large enough relative to the grid to maintain numerical stability [23]; ii) depending on the choice of grid resolution and a spanwise constant value of Gaussian radius, the predicted power may vary substantially [33]; and iii) that a blade-conforming $\varepsilon/c = $ constant yields improved results of the computed inflow distribution along an elliptic wing on stretched RANS-type grids [39]. In summary, the state-of-the-art in ALM suggests either a grid-based [23] or a chord-based [39] Gaussian radius ε.

In the following, we present a set of guidelines for choosing ALM parameters toward a consistent body-force representation on LES-type grids. As a first step, we state some requirements and bounds for ALM parameters on LES-type grids: (i) a relative grid spacing is approximately limited between $\Delta_{grid}/R = [1/30,\ 1/60]$ and is uniform along the actuator line to be both accurate and computationally feasible for using the ALM to model large wind farms using LES. (ii) The relative spacing between actuator points satisfies $\Delta_b/R \leq 1/20$ such that rotor thrust and power are computed accurately via integration over the actuator points along the blade radius (or span), a guideline used in general for BEM methods. (iii) It is hypothesized that an elliptic Gaussian radius ε along the actuator line complies with a first-order representation of a general blade loading. This hypothesis is the result of a simple thought experiment that a chord-based $\varepsilon/c = $ constant criterion is equivalent to a grid-based $\varepsilon/\Delta_{grid} = $ constant Gaussian radius if the blade has a rectangular planform. However, the blade may be appropriately twisted such that it achieves an elliptic blade loading, in which case the advantage of the chord-based $\varepsilon/c = $ constant criterion no longer applies.

各向同性网格

流体网格间距应该是半径的1/30或者1/60

激励点大于20个

分配半径的椭圆形分布是叶片载荷分布的一阶表达式。

对于矩形机翼而言，基于网格和基于弦长分布是等价的。但是实际由于叶片存在扭转，基于弦长的优势不复存在

The basic idea for the proposed guidelines was inspired by the "Schrenk Approximation" [41] used in the fixed-wing community to estimate the wing loading distribution during the aircraft design process. Here, we do not follow exactly Schrenk's methodology, but hypothesize that the Gaussian radius ε should be chosen based on an elliptic blade planform of the same aspect ratio as the actual blade, thus representing the first mode of the Fourier-series solution of a general blade loading. A methodology for finding the ALM parameters ε, Δ_{grid}, and Δ_b is described below:

(1) Determine the blade aspect ratio, AR

$$AR = \frac{R}{\bar{c}}; \quad \bar{c} = \frac{1}{R}\int_0^R c(r)dr \tag{4}$$

where R is the blade radius (or span) and $\bar{c}$ is the average blade chord.

(2) Find an "equivalent" elliptic planform with the same AR

$$c^*(r) = c_0\sqrt{1 - \left(\frac{2r}{R}\right)^2}; \quad c_0 = \frac{4}{\pi}\bar{c} \tag{5}$$

(3) Discretize the "equivalent" ellipse for given $\Delta_{grid}/R \leq 1/30$. Set minimum discretization levels as follows:

(a) $\varepsilon_{R/2} = n_{min}\Delta_{grid}$;
use $n_{min} = 1$ as a minimum discretization threshold on any given grid (6)

n_{min} need not be an integer.
Previous work by the authors [34] showed that $n_{min} = 0$ leads to numerical instabilities.

(b) $\varepsilon_0 = n_{max}\Delta_{grid}$; The value for n_{max} is determined from

$$n_{max}\frac{\Delta_{grid}}{R} \approx 0.08\ldots0.10 \tag{7}$$

Complying with $\Delta_{grid}/R \leq 1/30$, this results in $n_{max} \geq 3$ and leads to a consistent representation of the equivalent elliptic planform with grid refinement along the actuator line. n_{max} need not be an integer.
Using Eqs. (4), (5), and (7), postulate that

$$\varepsilon/c^* = \varepsilon_0/c_0 = 0.25\left(n_{max}\frac{\Delta_{grid}}{R}\right)(\pi AR) = \text{constant} \tag{8}$$

直接假设半径必须按照椭圆形分布

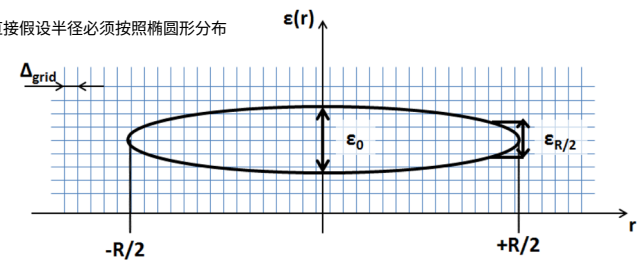

Fig. 3 Equivalent elliptic distribution of Gaussian radius, ε. Here, the equivalent blade ellipse that defines the Gaussian radius $\varepsilon(r)$ is shown on $-R/2 \leq r \leq +R/2$ for demonstration purposes only. For the actual computations of rotating blades and reporting the blade loads, the equivalent ellipse was shifted such that $0 \leq r \leq +R$.

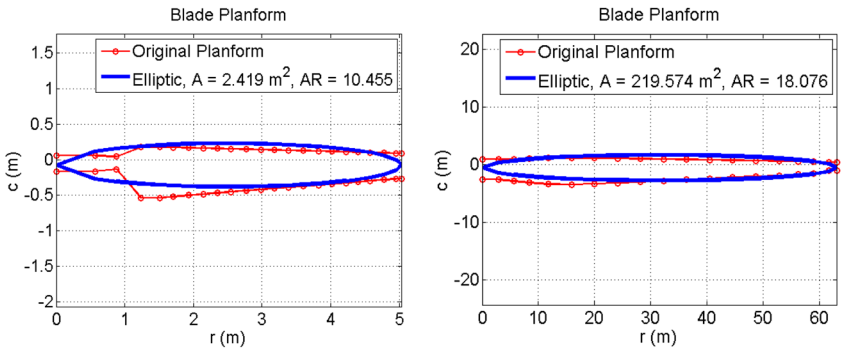

Fig. 4 Examples of the "equivalent" elliptic planform to define the Gaussian radius ε

while satisfying the minimum threshold of $\varepsilon(r) = \mathrm{MAX}(\varepsilon(r), \varepsilon_{R/2})$, see Fig. 3.

(4) Actuator spacing, $\Delta_b/\Delta_{\mathrm{grid}}$
It is recommended that the actuator spacing be chosen approximately such that

$$\Delta_b/\Delta_{\mathbf{grid}} \geq \mathbf{1.5} \tag{9}$$

激励点都定义子在叶元段的中间，其实梢部和底部端点是没有考虑的。

As the actuator line is discretized into segments and actuator points lie in the middle of the segments, there are no actuator points coincident with the tip and root. Equation (9) in conjunction with $\varepsilon_{R/2} = \Delta_{\mathrm{grid}}$ from Eq. (6) thus ensures that, when the Gaussian in Eq. (3) is used to project the actuator point force at the point adjacent to the blade tip and that adjacent to the root, the projected force at the actual tip and root is only 10% of its peak value at the adjacent actuator points. This assures that the body force does not extend appreciably beyond the location of the blade tip and root due to force projection with a three-dimensional Gaussian. Results presented in Sec. 3 will demonstrate that this is indeed advantageous in predicting blade tip loads. For the coarsest grid spacing of $\Delta_{\mathrm{grid}}/R = 1/30$, this results in $\Delta_b/R = 1/20$, which represents a minimum for blade-element integration.

Thus, for a given blade planform and grid that satisfy $\Delta_{\mathrm{grid}}/R \leq 1/30$, Eqs. (4)–(9) describe a general methodology for determining the most relevant ALM parameters, i.e., the Gaussian radius ε, the grid spacing Δ_{grid}, and the actuator spacing Δ_b. Figure 4 shows the "equivalent" elliptic planform areas c^* for the NREL Phase VI rotor blade and the NREL 5-MW turbine blade. It is important to note that the equivalent elliptic planform c^* is used solely for the purpose of defining the Gaussian radius ε along the blade span; the actual blade forces are computed using the actual blade chord distribution c.

等效弦长只用来分配作用力，剖面升力、阻力还是用原来的弦长计算的。

2.3 XTURB-PSU. An in-house developed wind turbine design and performance prediction code, XTURB-PSU [47,48], was used for a comparative study. XTURB-PSU uses either BEM theory based on NREL's AeroDyn code [49] or a prescribed helicoidal vortex method [50]. It also employs a stall delay model by Du and Selig [51] rooted in NREL's AirfoilPrep worksheet [52]. The XTURB-PSU code is used in BEM mode throughout this work to produce reference results for quantitative comparisons against the ALM with various spreading methods for the Gaussian radius ε.

延迟失速是叶片旋转带来的科氏力的结果

3 Results and Discussion

3.1 NREL Phase VI Rotor. Simulations were performed for the NREL Phase VI rotor [42] at a single wind speed of 7 m/s where the flow is attached along the entire blade. The NREL Phase VI rotor is a two-bladed stall-controlled wind turbine with 21.8 degrees of nonlinear twist and a blade-taper ratio of two. The NREL Phase VI rotor has been tested extensively in the NASA Ames 80×120 wind tunnel [42]. The blades are exclusively equipped with the S809 airfoil. Table 1 comprises some additional geometric parameters and operating conditions that are relevant to the ALM simulations. A total of 480 time steps per revolution was chosen as a baseline. The time step was chosen such that the blade tip does not traverse more than one grid cell per time step.

phase-VI是一个基于失速控制的两叶风机，最大扭角21.8度，叶片锥角2度

叶片每次计算不超过一个网格，每步0.75度

3.2 Grid-Based Gaussian Radius, $\varepsilon/\Delta_{\mathrm{grid}} = \mathrm{Constant}$. First, we want to demonstrate some of the shortcomings of using a constant Gaussian radius ε along the actuator line. Figure 5 shows ALM-computed AOAs along the blade for various constant Gaussian radii in comparison with results obtained by the XTURB-PSU code. Both the ALM and XTURB-PSU code use the same sectional S809 airfoil data along the blade span in the respective computations. The AOA distribution along the blade span is a quantitative measure of how well the blade inflow is predicted. Sectional lift

主要想说明：基于网格的固定分配半径有缺点

AOA的分布定量地表明了流体预估的准确性

Table 1 NREL phase VI rotor—geometric parameters and operating conditions

	NREL phase VI
Rotor radius, R (m)	5.029
Wind speed, $\mathbf{V}_{\mathbf{wind}}(m/s)$	7.0
Rotor speed (RPM)	72.0
Root cutout, r/R	0.0859

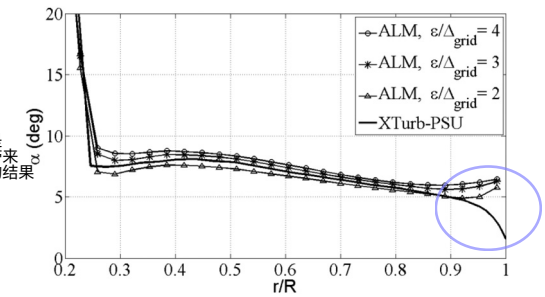

Fig. 5 Spanwise variation of AOA for the NREL phase VI rotor ($V_{\mathrm{wind}} = 7$ m/s). ALM parameters: $\varepsilon/\Delta_{\mathrm{grid}} = \mathrm{constant}$, $\Delta_{\mathrm{grid}}/R = 1/32$, $\Delta_b/\Delta_{\mathrm{grid}} = 1$.

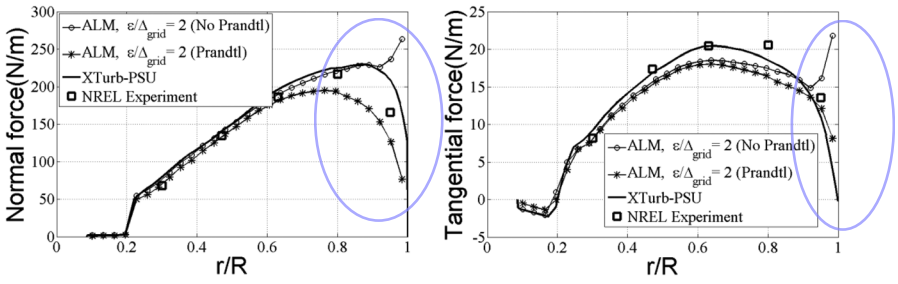

(a) Normal force per unit span, F_n 就是升力

(b) Tangential force per unit span, F_t 就是阻力

Fig. 6 Spanwise variation of force for the NREL phase VI rotor ($V_{wind} = 7$ m/s). ALM parameters: $\varepsilon/\Delta_{grid} = 2$, $\Delta_{grid}/R = 1/32$, $\Delta_b/\Delta_{grid} = 1$.

基于网格的固定分配半径在梢部结果偏大，减小分配系数对中部有一定改善，但梢部还是没用

and drag forces, which define the local blade force vector $\mathbf{f}_{N,m}$, strictly depend on the computed local AOA. It is quite apparent that a constant Gaussian radius complying with $\varepsilon/\Delta_{grid} = \text{constant}$ leads to a noticeable overprediction of blade tip loads. Furthermore, as $\varepsilon/\Delta_{grid}$ is reduced, the AOA distribution is shifted toward the reference case of XTURB-PSU results. This leads to an improved comparison at the midblade stations; however, the apparent overprediction of blade tip loads persists. 这么多？

Measured data for the sectional normal and tangential forces are available from NREL. Following the convention used in the NREL Phase VI experiment [42], the normal force acts orthogonal to the local chord line and toward the upper surface of the local airfoil section, while the tangential force acts in the local chord direction and toward the local leading edge. Figure 6 illustrates measured and computed sectional forces for a constant Gaussian radius $\varepsilon/\Delta_{grid} = 2$ with and without using the tip-loss factor due to Prandtl [35]. The Prandtl correction is applied locally to both the airfoil lift and drag coefficients. It has been implemented in exactly the same manner as the F1 correction described in Shen et al. [37]. The present work uses the Prandtl correction only in Fig. 6 in conjunction with a constant Gaussian radius ε. It can be seen that using Prandtl's correction leads to an underprediction of the blade tip loads compared with measured NREL data. This supports the notion that Prandtl's tip-loss factor is a somewhat artificial means of trying to improve ALM-computed blade tip loads when using a constant Gaussian radius ε. The authors wish to note that the Prandtl correction was originally developed for BEM-type computations of propeller loads.

prandtl修正是结果偏低，它本身就是个经验公式

In general, there should be no need for using the Prandtl correction within the ALM framework, since the three-dimensional flow field containing tip and root vortices is fully resolved by the ALM. Table 2 comprises computed rotor power and thrust in comparison with XTURB-PSU and measured data from NREL. For the case of $\varepsilon/\Delta_{grid} = 2$ in Fig. 6, the rotor power predicted by ALM is 4.26% larger than that computed by XTURB-PSU and 5.47% larger than the data. The case with the Prandtl correction exhibits closer agreement with the trends of XTURB-PSU and the data toward the blade tip. It is apparent from Table 2, though, that using the Prandtl correction leads to underprediction of the integrated power and thrust. The Prandtl correction is not used for the remainder of this paper unless otherwise noted.

由于AL完全解析了流体和梢涡，应该可以不需要修正。

Table 2 Rotor power and thrust—NREL phase VI rotor ($V_{wind} = 7$ m/s); ALM parameters: $\varepsilon/\Delta_{grid} = \text{constant}$, $\Delta_{grid}/R = 1/32$, $\Delta_b/\Delta_{grid} = 1$

NREL phase VI rotor	Power (W)	Thrust (N)
NREL experiment	6,030	1,120
XTurb-PSU	6,100	1,240
ALM ($\varepsilon/\Delta_{grid} = 4.0$)	7,390	1,405
ALM ($\varepsilon/\Delta_{grid} = 3.0$)	7,100	1,380
ALM ($\varepsilon/\Delta_{grid} = 2.0$)	6,360	1,310
ALM ($\varepsilon/\Delta_{grid} = 2.0$, Prandtl factor)	5,520	1,090

3.3 Chord-Based Gaussian Radius, $\varepsilon/c = \text{Constant}$. The recent work of Shives and Crawford [39] suggests a Gaussian radius of $\varepsilon/c = 0.25$ with $\varepsilon/\Delta_{grid} \geq 4$ based on a test case of an elliptic wing of AR = 10.2 and computed with a RANS solver on stretched grids. For the NREL Phase VI rotor with $c_{min}/R = 0.0707$ at the blade tip, this would require a grid spacing of $\Delta_{grid}/R = 1/226$ assuming a LES-type grid with a cell aspect ratio of unity. There is no doubt that such a high grid resolution along the actuator line is not feasible for ABL-LES simulations of large wind farms using the ALM. However, Shives and Crawford also state that their criteria may be to some extent specific to the solver used for the simulations. Allowing a larger cell aspect ratio in the ABL-LES simulations around the actuator line in conjunction with higher values for ε/c, the criteria suggested by Shives and Crawford may be relaxed.

基于弦长的做法，网格分辨率要求太高

We investigate this by choosing a typical grid spacing of $\Delta_{grid}/R = 1/37$ used in wind farm simulations involving the ALM. The criterion $n_{max}(\Delta_{grid}/R) \approx 0.08 \ldots 0.10$ in Eq. (7) hence results in $n_{max} = 3, 4$ as upper and lower discretization limits. For the given grid and rotor dimensions, values for ε/c were obtained such that $\varepsilon/c = n_{max}\,\Delta_{grid}/\,c_{max}$ with $n_{max} = 3, 4$ with reference to Eq. (7). For the NREL Phase VI rotor, $c_{max}/R \approx 0.14$ so that $\varepsilon/c = 0.57$ for $n_{max} = 3$ and $\varepsilon/c = 0.76$ for $n_{max} = 4$. Furthermore, we find that $c_{tip}/c_{max} \approx 1/2$ for the NREL Phase VI rotor. Hence the Gaussian radius ε at the tip becomes $\varepsilon_{tip} = 1.5\Delta_{grid}$ and $2.0\Delta_{grid}$, respectively. Figure 7 shows computed AOA versus blade span for $\varepsilon/c = 0.57$, 0.76 in comparison with results obtained by the blade-element based XTURB-PSU code. It can be seen in Fig. 7 that reducing ε/c improves the comparison against results obtained by XTURB-PSU. For the given grid, though, $\varepsilon/c = 0.57$ is near the lower discretization limit of the projection function. The overprediction of blade tip loads is still apparent, similar to the grid-based Gaussian radii from Figs. 5 and 6. In the following, we vary the actuator spacing Δ_b/Δ_{grid} with the idea of reducing the overlap regions of the volumetric body-force distribution around an actuator point.

基于弦长的分配方法依然存在梢部估计偏大的问题

Figure 8 reveals that increasing the actuator spacing has a small, though positive, effect on predicting the blade tip loads. 点的间距对结果影响很小，作者认为是：梢部力的重叠导致尾涡强度变低，从而下洗角变小，从而AOA偏大，力偏大

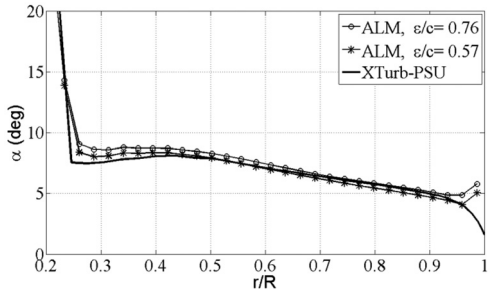

Fig. 7 Spanwise variation of AOA for the NREL phase VI rotor ($V_{wind} = 7$ m/s). ALM parameters: $\varepsilon/c = \text{constant}$, $\Delta_{grid}/R = 1/37$, $\Delta_b/\Delta_{grid} = 1$.

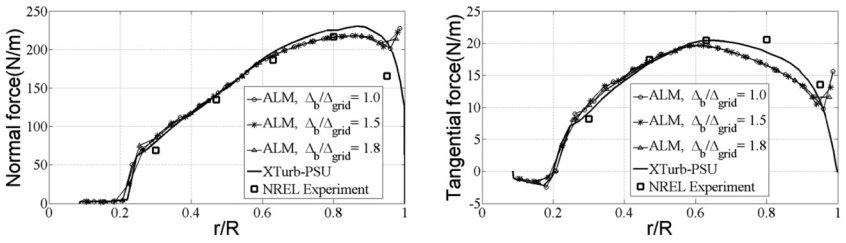

(a) Normal force per unit span, F_n (b) Tangential force per unit span, F_t

Fig. 8 Spanwise variation of force for the NREL phase VI rotor (V_{wind} = 7 m/s). ALM parameters: $\varepsilon/c = 0.57$, $\Delta_{grid}/R = 1/37$, Δ_b/Δ_{grid} = constant.

Table 3 Rotor power and thrust—NREL phase VI rotor (V_{wind} = 7 m/s); ALM parameters: $\varepsilon/c = 0.57$, $\Delta_{grid}/R = 1/37$, Δ_b/Δ_{grid} = constant

NREL phase VI rotor	Power (W)	Thrust (N)
NREL experiment	6,030	1,120
XTurb-PSU	6,100	1,240
ALM ($\Delta_b/\Delta_{grid} = 1.0$)	6,170	1,280
ALM ($\Delta_b/\Delta_{grid} = 1.5$)	6,210	1,290
ALM ($\Delta_b/\Delta_{grid} = 1.8$)	6,105	1,275

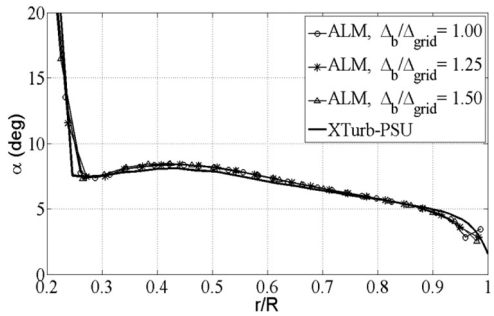

Fig. 9 Spanwise variation of AOA for the NREL phase VI rotor (V_{wind} = 7 m/s). ALM parameters: $\varepsilon/c^* = 0.67$, $\Delta_{grid}/R = 1/37$, Δ_b/Δ_{grid} = constant.

The reason for this observation is believed to be related to the strength of the trailing vorticity emanating from the actuator line between the two actuator points closest to the blade tip. If the Gaussian radius ε is too large compared with the actuator spacing Δ_b, then adjacent overlapping force distributions may lower the strength of the trailing vorticity and hence induce less downwash at the actuator line that leads to the observed overprediction in the AOA close to the blade tip. For $\varepsilon_{tip} = 1.5\ \Delta_{grid}$ in Fig. 8, the Gaussian in Eq. (3) has reduced to 0.64 of its peak strength at the adjacent inboard actuator point for $\Delta_b/\Delta_{grid} = 1.0$ ($\varepsilon = 1.5\ \Delta_{grid}$ and $|r| = 1.0\ \Delta_{grid}$ in Eq. (3)). Similarly, the Gaussian reduces to 0.37 and 0.24, respectively, for $\Delta_b/\Delta_{grid} = 1.5$ and 1.8. As noted earlier, a small improvement can be seen in the tip-load prediction in Fig. 8; however, one has to be aware that $\Delta_b/\Delta_{grid} = 1.8$ results in $\Delta_b/R \approx 1/20$ (or 20 actuator points along the actuator line), which can be considered a minimum requirement for the number of blade elements along an actuator (or lifting) line.

分配力的重叠可能会降低尾涡强度，从而减小上游的下洗角，进而导致梢部攻角的结果偏大

Computed rotor power and thrust are summarized in Table 3. Maximum discrepancies between results obtained by XTURB-PSU and ALM amount to 1.8% for the rotor power and 4.0% for the rotor thrust for the ALM run with $\Delta_b/\Delta_{grid} = 1.5$. Figure 8 supports, however, that the close agreement between XTURB-PSU and ALM results is an artifact of cancelling spanwise underprediction and overprediction of blade loads.

3.4 Elliptic Gaussian Radius, ε/c^* = Constant (General Guidelines for ALM Parameters). In the following, we demonstrate that the proposed method in Sec. 2 for determining the ALM parameters ε, Δ_{grid}, and Δ_b leads to improved and consistent results for various computational grids. Figure 9 shows that an elliptic Gaussian radius ε determined by the guidelines in Sec. 2 results in AOA prediction very comparable with the XTURB-PSU results. For a standard actuator spacing of $\Delta_b/\Delta_{grid} = 1.0$, however, the AOA at the blade tip is still overpredicted in comparison with XTURB-PSU. Increasing Δ_b/Δ_{grid} for $\varepsilon_{tip} = \varepsilon_{R/2} = \Delta_{grid}$ according to Eq. (6), the Gaussian in Eq. (3) reduces to 0.21 ($\Delta_b/\Delta_{grid} = 1.25$) and 0.11 ($\Delta_b/\Delta_{grid} = 1.50$) of its peak value at the adjacent actuator point, and eliminates the overprediction of AOA at the blade tip. It is apparent in Fig. 9 that the elliptic Gaussian radius ε governed by Eq. (8) for $n_{max} = 3$ results in an improved AOA prediction compared with a grid-based or chord-based Gaussian radius.

增大剖面间距，消除了AOA的重叠

Next, we show that the general guidelines for ALM parameters described in Sec. 2 predict consistent tip loads for variable grid spacing Δ_{grid}/R. Figure 10 shows computed sectional normal and tangential forces using the general guidelines for ALM parameters defined in Sec. 2 in comparison with results computed by XTURB-PSU and measured NREL data. It can be seen that consistent predictions are obtained when following the general guidelines for the ALM parameters barring some load overprediction for all grids. For all cases, $\varepsilon_{tip} = \varepsilon_{R/2} = \Delta_{grid}$ was used according to

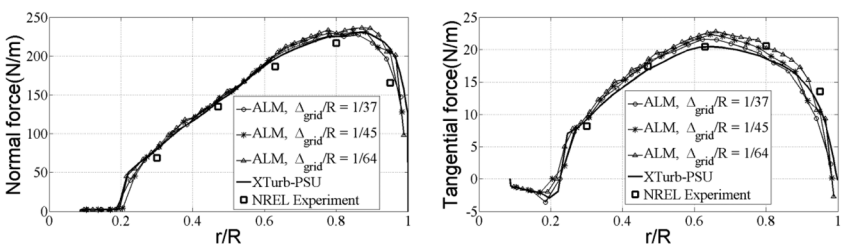

(a) Normal force per unit span, F_n (b) Tangential force per unit span, F_t

Fig. 10 Spanwise variation of force for the NREL phase VI rotor (V_{wind} = 7 m/s). ALM parameters: $\varepsilon/c^* = 0.67$, Δ_{grid}/R = constant, $\Delta_b/\Delta_{grid} = 1.5$.

Table 4 Rotor power and thrust—NREL phase VI rotor ($V_{wind} = 7$ m/s); ALM parameters: $\varepsilon/c^* = 0.67$, $\Delta_{grid}/R =$ constant, $\Delta_b/\Delta_{grid} = 1.5$

NREL phase VI rotor	Power (W)	Thrust (N)
NREL experiment	6,030	1,120
XTurb-PSU	6,100	1,240
ALM ($\Delta_{grid}/R = 1/37$)	6,210	1,280
ALM ($\Delta_{grid}/R = 1/45$)	6,310	1,290
ALM ($\Delta_{grid}/R = 1/64$)	6,615	1,315
ALM ($\Delta_{grid}/R = 1/45$, $n_{min} = 1.2$)	6,340	1,300
ALM ($\Delta_{grid}/R = 1/64$, $n_{min} = 1.7$)	6,570	1,325

Eq. (6). For a reference grid of $\Delta_{grid}/R = 1/37$, we choose $n_{max} = 3$ so that $n_{max}\ \Delta_{grid}/R = 0.081$ satisfies Eq. (7). As the grid spacing Δ_{grid}/R is refined, n_{max} is increased accordingly. Equation (8) hence results in $\varepsilon/c^* = 0.67$ for a blade aspect ratio of AR = 10.54. Furthermore, the time step Δt is reduced with grid refinement such that the actuator line never traverses more than one grid cell per time step.

In Fig. 10, computed ALM results are very close to those obtained by XTURB-PSU. In particular, the blade tip loads show improved agreement compared with a grid-based or chord-based Gaussian radius ε. There is still some apparent discrepancy between computed and measured NREL data. At this stage, this is attributed to some inaccuracy in the airfoil tables used for the ALM and XTURB-PSU computations. The airfoil tables for the S809 airfoil were obtained exclusively from the computer program XFOIL at various Reynolds numbers and without any modifications to the built-in transition criterion within XFOIL. The authors had decided not to use experimental data because previous work [53] had shown apparent differences in measured S809 airfoil characteristics obtained in different facilities that are not easy to assess. It was found, though, [53] that XFOIL is capable of predicting the S809 airfoil characteristics very well within the experimental data range. Furthermore, no corrections that account for blade rotation and three-dimensionality [51] were added to the airfoil tables in order not to introduce additional empiricism that would distract from the main objective of this work. It is apparent from the obtained ALM results that the proposed general guidelines show improved comparison to computed XTURB-PSU and measured NREL data than those obtained with a grid-based or chord-based Gaussian radius ε.

Although the load distributions in Fig. 10 are quite consistent, integrated rotor power and thrust in Table 4 seem to have not yet reached a converged state with respect to grid refinement. For the ALM run with $\Delta_{grid}/R = 1/64$, the rotor power computed by ALM is 8.4% higher and the rotor thrust 6.0% higher compared with results obtained by XTURB-PSU. For the ALM runs in Fig. 10 and Table 4, n_{max} was scaled according to Eq. (7) as the grid was refined. However, $n_{min} = 1$ was kept constant for all ALM runs using Eq. (6) of the general guidelines as a minimum

Table 5 NREL 5-MW turbine—geometric parameters and operating conditions

	NREL 5-MW
Rotor radius, R (m)	63
Wind speed, V_{wind} (m/s)	8.0
Rot. speed (RPM)	9.156
Root cutout, r/R	0.0238

discretization level on a given grid. Hence, the Gaussian radius ε has a slightly different distribution near the blade tips for each case. It was therefore investigated whether scaling n_{min} according to n_{max}, i.e., having exactly the same physical $\varepsilon(r)$ between grids, would affect integrated rotor power and thrust. The corresponding results in Table 4 for $n_{min} = 1.2$ on the grid with $\Delta_{grid}/R = 1/45$ and $n_{min} = 1.7$ on the grid with $\Delta_{grid}/R = 1/64$ show in comparison with their counterparts on the same grid with $n_{min} = 1$ that the effect is only on the order of 1%. This actually supports the use of Eq. (6) with $n_{min} = 1$ on any given grid. It is worth mentioning in this context that a previous study [33] has shown a similar trend in ALM computed power with grid refinement where it was found that the computed rotor power is converged to within approximately two percent for grids finer than $\Delta_{grid}/R = 1/64$. The computational grid was therefore not refined beyond this resolution.

Figure 11 presents the local AOA α and the square of the local velocity magnitude V^2_{mag}, both of which contribute directly to sectional forces. It can be seen that both quantities have nearly converged. It is true, though, that rotor thrust and, in particular, rotor power are very sensitive to small changes in the respective quantities.

3.5 NREL 5-MW Turbine. The NREL 5-MW turbine [40] is a notional offshore wind turbine design. Hence, measured data are not available for this wind turbine. However, the NREL 5-MW turbine becomes an increasingly popular test case for actuator-type wind farm simulations. Some geometric parameters and operating conditions are given in Table 5. In this work, we performed ALM simulations with various parameter settings for the NREL 5-MW turbine. As was done for the NREL Phase VI rotor, the time step Δt was chosen such that the blade tip does not traverse more than one grid cell per time step. As the grid is refined, the time step is scaled down accordingly, which follows the way in which the ALM is used in practice.

The NREL 5-MW turbine has a blade aspect ratio of AR = 18.1, which is significantly larger than that of the NREL Phase VI rotor. It is therefore a good test case for the proposed ε/c^* criterion in Eq. (8). We choose two grid spacings along the actuator line, i.e., $\Delta_{grid}/R = 1/32$ and $1/64$, that define commonly used bounds for LES simulations of large wind farms. For $\Delta_{grid}/R = 1/32$, we choose $n_{max} = 3$ so that $n_{max}\ \Delta_{grid}/R$ satisfies Eq. (7). Hence $n_{max} = 6$ is chosen for $\Delta_{grid}/R = 1/64$, respectively. Equation (8) thus gives $\varepsilon/c^* = 1.33$. Computed sectional normal and tangential forces are shown in Fig. 12. The force convention again

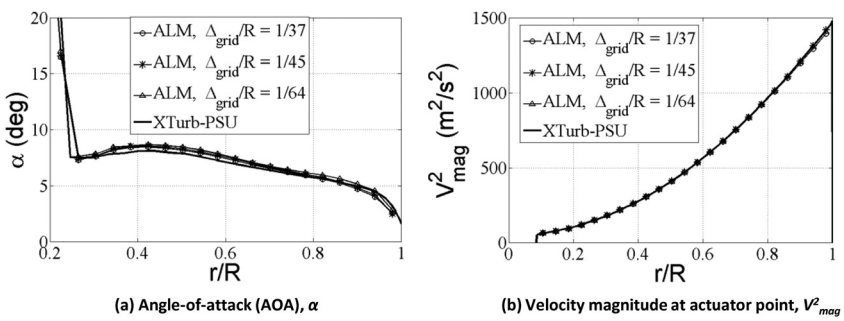

(a) Angle-of-attack (AOA), α (b) Velocity magnitude at actuator point, V^2_{mag}

Fig. 11 Spanwise variation of AOA and velocity magnitude for the NREL phase VI rotor ($V_{wind} = 7$ m/s). ALM parameters: $\varepsilon/c^* = 0.67$, $\Delta_{grid}/R =$ constant, $\Delta_b/\Delta_{grid} = 1.5$.

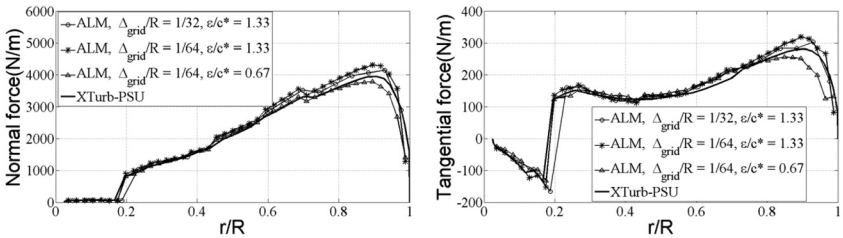

(a) Normal force per unit span, F_n (b) Tangential force per unit span, F_t

Fig. 12 Spanwise variation of force for the NREL 5-MW turbine (V_{wind} = 8 m/s). ALM parameters: ε/c^* = 1.33, 0.67, Δ_{grid}/R = constant, Δ_b/Δ_{grid} = 1.5.

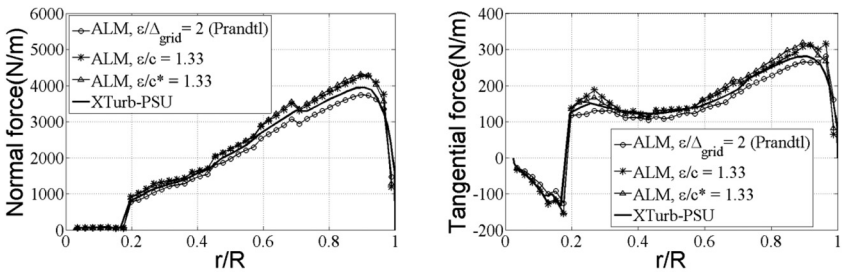

(a) Normal force per unit span, F_n (b) Tangential force per unit span, F_t

不同方法的对比

Fig. 13 Spanwise variation of force for the NREL 5-MW turbine (V_{wind} = 8 m/s). ALM parameters: Δ_{grid}/R = 1/64.

Table 6 Rotor power and thrust—NREL 5-MW turbine (V_{wind} = 8 m/s); ALM parameters: ε, Δ_{grid}/R = 1/64

NREL 5-MW turbine	Power (kW)	Thrust (kN)
XTurb-PSU	1,890	384
ALM ($\varepsilon/\Delta_{grid} = 2$, Prandtl factor)	1,737	358
ALM ($\varepsilon/c = 1.33$)	2,066	403
ALM ($\varepsilon/c^* = 1.33$)	2,113	409

follows NREL's definition [42] where the normal force acts orthogonal to the local chord line and toward the sectional airfoil's upper surface, while the tangential force is parallel to the local chord line and oriented toward the leading edge. It can be seen that the shape of the loading profiles along the span is consistent and behaves properly at the tips when using the ALM parameters chosen according to the guidelines developed in Sec. 2. However, it is apparent that using $\varepsilon/c^* = 1.33$ with both grid resolutions creates larger loads than predicted with XTURB-PSU. For comparison, a case for $\varepsilon/c^* = 0.67$ is also shown, and it can be seen that

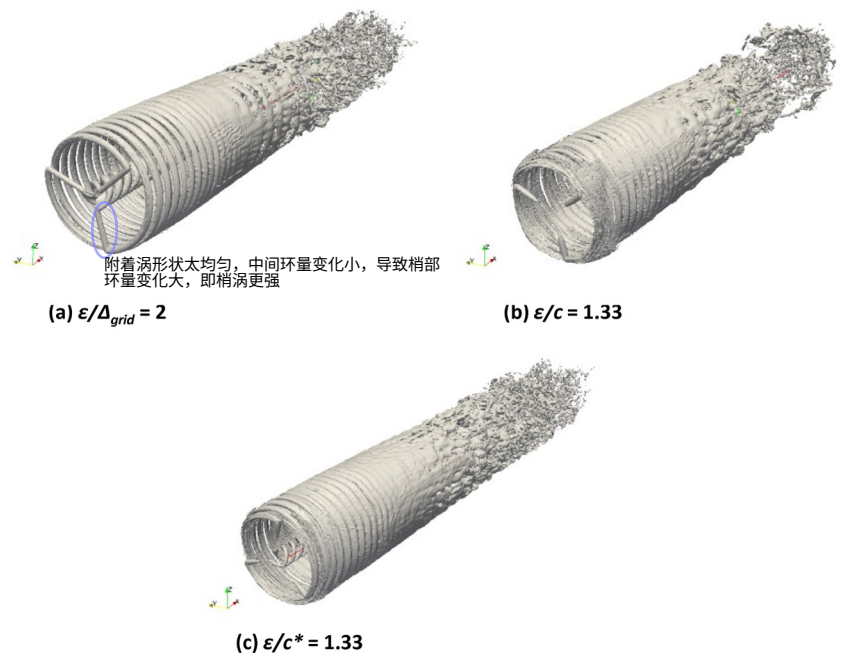

附着涡形状太均匀，中间环量变化小，导致梢部环量变化大，即梢涡更强

(a) $\varepsilon/\Delta_{grid}$ = 2 (b) ε/c = 1.33

(c) ε/c^* = 1.33

Fig. 14 Wake structure and strength for the NREL 5-MW turbine (V_{wind} = 8 m/s) showing isosurface of vorticity magnitude 0.5 s^{-1}

computed loads are too low, especially near the sensitive tip region. This clearly demonstrates that the value of ε/c^* is a function of the blade aspect ratio, as suggested by Eq. (8). However, the fact that using $\varepsilon/c^* = 1.33$ or $\varepsilon/c^* = 0.67$ overpredicts or underpredicts, respectively, blade loads across the entire span compared with XTURB-PSU suggests that the guideline provided in Eq. (7) for choosing the value of n_{max} is not a hard rule, but a mere guideline. It is only through future work, possibly with application to other rotors, that a more precise means of computing n_{max} can be found.

As a final investigation, we apply best-practices for a grid-based, chord-based, and elliptic Gaussian radius ε to the NREL 5-MW turbine using $\Delta_{grid}/R = 1/64$. The Prandtl correction was only used for the best-practice case of a grid-based Gaussian radius ε. The results are presented in Fig. 13. In comparison with the NREL Phase VI rotor, a chord-based Gaussian radius $\varepsilon/c =$ constant exhibits improved results. This is attributed to the fact that the chord distribution near the blade tip of the NREL 5-MW turbine is not too different from an elliptic shape, see Fig. 4(*b*). It is clear, though, that the proposed elliptic Gaussian radius with $\varepsilon/c^* =$ constant gives consistent results between various blade designs and grid spacing. It is therefore a more general method for determining ALM parameters. In particular, it suggests a suitable value for ε/c^* for a given grid resolution Δ_{grid}/R and blade aspect ratio AR. Table 6 summarizes computed rotor power and thrust for the best-practice cases in Fig. 13. The wake structure, characteristic of the momentum deficit, corresponding to the results in Fig. 13 is presented in Fig. 14. The advantage of using the proposed method of Gaussian spreading is evident. It can be seen that both tip and root vortices appear tighter for the case of a variable Gaussian radius ε along the blade span. Furthermore, the bound vorticity along the blade is less tubelike and appears to have more of an elliptic shape.

5 MW的梢部弦长本身就接近于弦长分布

附着涡也更像一个椭圆，而不是管

4 Summary and Conclusions

The ALM within ABL-LES solvers is increasingly used as the evolving standard for the computation of wake interactions in large wind farms. As of today, however, no general guidelines exist for choosing ALM modeling parameters on LES-type grids. The main contribution of this work is the development and testing of a much-needed set of guidelines to determine the most important ALM parameters, i.e., the Gaussian radius ε, the grid resolution Δ_{grid}/R, and the actuator spacing Δ_b/Δ_{grid}. An elliptic spanwise distribution of the Gaussian radius ε is proposed along the blade where the equivalent elliptic planform c^* has the same aspect ratio than the actual blade. With reference to Schrenk's approximation used in the fixed-wing community, this represents a first-order approximation of the actual blade loading and defines a constant value for ε/c^* along the blade that predominantly depends on the grid resolution and the blade aspect ratio.

The new set of guidelines for determining ALM parameters was tested for the NREL Phase VI rotor and the NREL 5-MW turbine. For the NREL Phase VI rotor, it was first demonstrated that the current best-practice of a grid-based Gaussian radius $\varepsilon/\Delta_{grid} =$ constant leads to an overprediction of blade tip loads; hence, rotor power and thrust are not necessarily correct. Furthermore, the value of $\varepsilon/\Delta_{grid}$ could be tuned to give the correct power and thrust, which are integrated quantities, but the spanwise distribution of loading would not have the proper shape. A recent idea of using a chord-based Gaussian radius $\varepsilon/c =$ constant was also shown not to solve the apparent issue of overpredicting blade tip loads for the NREL Phase VI rotor; however, there was some improvement compared with the grid-based $\varepsilon/\Delta_{grid} =$ constant. As for the proposed guidelines that involve an elliptic Gaussian radius $\varepsilon/c^* =$ constant along the actuator line, good comparisons were obtained against measured NREL data and results computed by the BEM-based XTURB-PSU code using the same airfoil tables as the ALM simulations. Given the airfoil tables, the ALM results obtained with the proposed guidelines are believed to be as close to measured NREL data as the unmodified airfoil tables allow. It should be noted, though, that the NREL Phase VI rotor blade has tips of finite chord (the rotor does not elliptically approach zero chord length at the tip); however, it exhibits more of an elliptic-shaped loading. The $\varepsilon/c =$ constant force projection reflects the chord distribution and not the load distribution, so it is understandable that the method is in error and highlights a common blade geometry upon which that method does not work as well as the $\varepsilon/c^* =$ constant projection. For the NREL 5-MW turbine, no data are available, and quantitative comparisons of ALM-computed blade loads along with rotor power and thrust were performed against results obtained by the XTURB-PSU code. It was shown that the proposed guidelines for ALM parameters rooted in an elliptic Gaussian radius ε/c^* show consistent and good results for blade loads as well as rotor power and thrust on various LES-type grids used in large wind farm wake simulations.

In conclusion, the proposed guidelines for ALM parameters on LES-type grids have proven to give consistent and good comparisons and thus provide the wind energy community with a useful and much-needed methodology to model wind turbine wakes as accurately as embedded airfoil data tables allow. The ALM computations for the NREL 5-MW turbine suggest, however, that some future work is needed to provide a tighter criterion for Eq. (7) of this work that relates the maximum spreading radius parameter to the grid spacing as the product $n_{max}\ \Delta_{grid}/R$. It is surmised that application to other wind turbine rotors by the wind energy community will provide more precise values for this product. The main contribution of this work has been to develop and test the idea of an elliptic Gaussian radius along the blade span that accounts for a consistent and correct distribution of blade loads along the actuator line. Additional future research will be directed toward investigating how sensitive turbine wake characteristics, such as the spatial evolution of the wake momentum deficit downstream and wake turbulence statistics, are to ALM parameters determined by the current and new proposed guidelines.

Acknowledgment

This work was supported by the Department of Energy (DE-EE0005481) as part of the "Cyber Wind Facility" project at The Pennsylvania State University and in collaboration with NREL.

Nomenclature

ABL = atmospheric boundary layer
ADM = actuator disk method
ALM = actuator line method
AOA = angle of attack (deg)
AR = blade aspect ratio
BEM = blade-element momentum
c = airfoil chord (m)
CFD = computational fluid dynamics
D = turbine rotor diameter (m)
F_n = sectional normal force (N/m)
F_t = sectional tangential force (N/m)
LES = large-eddy simulation
NREL = National Renewable Energy Laboratory
OPENFOAM = Open field operations and manipulations
R = blade radius (m)
RANS = Reynolds-averaged Navier–Stokes
RPM = revolutions per minute (1/min)
V_{wind} = mean wind speed (m/s)
Δ_b = actuator width (m)
Δ_{grid} = grid resolution (m)
ε = radius of the body-force projection function (m)

References

[1] "20% Wind Energy by 2030," 2008, US Department of Energy Executive summary, DOE/GO-102008-2578, December 2008.

[2] "Eastern Wind Integration and Transmission Study," 2011, prepared for the National Renewable Energy Laboratory by the EnerNex Corporation, Report No. NREL/SR-5500-47078, February 2011.
[3] "Western Wind and Solar Integration Study," 2010, prepared for the National Renewable Energy Laboratory by GE Energy, Report No. NREL/SR-550-47434, May 2010.
[4] Churchfield, M. J., Lee, S., Michalakes, J., and Moriarty, P. J., 2012, "A Numerical Study of the Effects of Atmospheric and Wake Turbulence on Wind Turbine Dynamics," J. Turbulence, **13**(12), pp. 1–32.
[5] Jensen, L. E., 2007, "Array Efficiency at Horns Rev and the Effect of Atmospheric Stability," Dong Energy, Fredericia, Denmark.
[6] Kelley, N. D., 2011, "Turbulence-Turbine Interactions: The Basis for the Development of the TurbSim Stochastic Simulator," National Renewable Energy Laboratory, Golden, CO, Report No. NREL/TP-5000-52353.
[7] Katic, I., Hoejstrup, J., and Jensen, N. O., 1986, "A Simple Model for Cluster Efficiency," European Wind Energy Association (EWEC'86), Rome, Italy, October 7–9, pp. 407–410.
[8] Rathmann, O., Frandsen, S. T., and Barthelmie, R. J., 2007, "Wake Modelling for Intermediate and Large Wind Farms," European Wind Energy Conference and Exhibition, Milan, Italy, May 7–10.
[9] "WAsP—The Wind Atlas Analysis and Application Program," 2013, Risoe National Laboratory for Sustainable Energy, Roskilde, Denmark, retrieved on April 23, 2013, http://www.wasp.dk/Products/WAsP.aspx
[10] Crespo, A., Hernandez, J., Fraga, E., and Andreu, C., 1988, "Experimental Validation of the UPM Computer Code to Calculate Wind Turbine Wakes and Comparison With Other Models," J. Wind Eng. Ind. Aerodyn., **27**, pp. 77–88.
[11] Sørensen, J. N., Shen, W. Z., and Munduate, X., 1998, "Analysis of Wake States by a Full-Field Actuator Disc Model," Int. J. Numer. Methods Fluids, **1**, pp. 73–78.
[12] Leclerc, C., and Masson, C., 2004, "Toward Blade-Tip Vortex Simulation With an Actuator-Lifting Surface Model," AIAA Paper No. 2004-0667.
[13] Leclerc, C., and Masson, C., 2005, "Wind Turbine Performance Predictions Using a Differential Actuator-Lifting Disk Model," ASME J. Sol. Energy Eng., **127**, pp. 200–208.
[14] Réthoré, P. E., Sørensen, N. N., and Zahle, F., 2010, *Validation of an Actuator Disc Model*, European Wind Energy Conference & Exhibition (EWEC), Warsaw, Poland, April 20–23.
[15] Mikkelsen, R., 2003, "Actuator Disc Methods Applied to Wind Turbines," Ph.D. thesis, Technical University of Denmark, Lyngby, Denmark.
[16] Ivanell, S., Mikkelsen, R., Sørensen, J., and Henningson, D., 2009, "ACD Modelling of Wake Interaction in the Horns Rev Wind Farm," *Extended Abstracts for Euromech Colloquium 508 on Wind Turbine Wakes*, European Mechanics Society, Madrid, Spain.
[17] Meyers, J., and Meneveau, C., 2010, "Large Eddy Simulations of Large Wind-Turbine Arrays in the Atmospheric Boundary Layer," AIAA Paper No. 2010-0827.
[18] Singer, M., Mirocha, J., Lundquist, J., and Cleve, J., 2010, "Implementation and Assessment of Turbine Wake Models in the Weather Research and Forecasting Model for Both Mesoscale and Large-Eddy Simulation," International Symposium on Computational Wind Engineering, Chapel Hill, NC, May 23–27, Paper No. LLNL-CONF-425048.
[19] Stovall, T. D., Pawlas, G., and Moriarty, P. J., 2010, "Wind Farm Wake Simulations in OpenFOAM," AIAA Paper No. 2010-0825.
[20] Sørensen, J. N., and Shen, W. Z., 2002, "Numerical Modeling of Wind Turbine Wakes," ASME J. Fluids Eng., **124**, pp. 393–399.
[21] Troldborg, N., 2008, "Actuator Line Modeling of Wind Turbine Wakes," Ph. D. thesis, Technical University of Denmark, Lyngby, Denmark.
[22] Troldborg, N., Sørensen, J. N., and Mikkelsen, R., 2007, "Actuator Line Simulation of Wake of Wind Turbine Operating in Turbulent Inflow," J. Phys.: Conf. Ser., **75**, p. 012063.
[23] Troldborg, N., Sørensen, J., and Mikkelsen, R., 2010, "Numerical Simulations of Wake Characteristics of a Wind Turbine in Uniform Flow," Wind Energy, **13**, pp. 86–99.
[24] Sibuet Watters, C., and Masson, C., 2010, "Modelling of Lifting-Device Aerodynamics Using the Actuator Surface Concept," Int. J. Numer. Methods Fluids, **62**(11), pp. 1264–1298.
[25] Lu, H., and Porté-Agel, F., 2011, "Large-Eddy Simulation of a Very Large Wind Farm in a Stable Atmospheric Boundary Layer," Phys. Fluids, **23**, p. 065101.
[26] Conzemius, B., Lu, H., Chamorro, L., Wu, Y.-T., and Porte-Agel, F., 2010, "Development and Testing of a Wind Farm Simulator at an Operating Wind Farm," AWEA 2010 Wind Power Conference and Exhibition, Dallas, TX, May 23–26.
[27] OpenFOAM, 2012, ESI Group-OpenCFD, Ver. 2.0.x, retrieved on Dec. 13, 2012, http:// www.openfoam.org/git.php
[28] Churchfield, M. J., Moriarty, P. J., Vijayakumar, G., and Brasseur, J., 2010, "Wind Energy-Related Atmospheric Boundary-Layer Large-Eddy Simulation Using OpenFOAM," National Renewable Energy Laboratory, Golden, CO, Report No. NREL/CP-500-48905.
[29] Churchfield, M. J., 2011, "Wind Energy/Atmospheric Boundary Layer Tools and Tutorials," 6th OpenFOAM Workshop, The Pennsylvania State University, State College, PA, June 13–16.
[30] Churchfield, M. J., Lee, S., Moriarty, P. J., Martínez, L. A., Leonardi, S., Vijayakumar, G., and Brasseur, J. G., 2012, "A Large-Eddy Simulation of Wind-Plant Aerodynamics," AIAA Paper No. 2012-0537.
[31] Dobrev, I., Massouh, F., and Rapin, M., 2007, "Actuator Surface Hybrid Model," J. Phys. Conf. Ser., **75**, p. 012019.
[32] Shen, W. Z., Zhang, J. H., and Sorensen, J. N., 2009, "The Actuator Surface Model: A New Navier-Stokes Based Model for Rotor Computations," ASME J. Sol. Energy Eng., **131**(1), p. 011002.
[33] Martínez, L. A., Leonardi, S., Churchfield, M. J., and Moriarty, P. J., 2012, "A Comparison of Actuator Disk and Actuator Line Wind Turbine Models and Best Practices for Their Use," AIAA Paper No. 2012-0900.
[34] Jha, P. K., Churchfield, M. J., Moriarty, P. J., and Schmitz, S., 2013, "Accuracy of State-of-the-Art Actuator-Line Modeling for Wind Turbine Wakes," AIAA Paper No. 2013-0608.
[35] Glauert, H., 1985, *Airplane Propellers*, Dover, New York, pp. 251–268.
[36] Shen, W. Z., Zhu, W. J., and Sørensen, J. N., 2012, "Actuator Line/Navier-Stokes Computations for the MEXICO Rotor: Comparison With Detailed Measurements," Wind Energy, **15**(5), pp. 811–825.
[37] Shen, W. Z., Mikkelsen, R., Sørensen, J. N., and Bak, C., 2005, "Tip Loss Corrections for Wind Turbine Computations," Wind Energy, **8**(4), pp. 457–475.
[38] Shen, W. Z., Sørensen, J. N., and Mikkelsen, R., 2005, "Tip Loss Corrections for Actuator/Navier-Stokes Computations," ASME J. Sol. Energy Eng., **127**(2), pp. 209–213.
[39] Shives, M., and Crawford, C., 2012, "Mesh and Load Distribution Requirements for Actuator Line CFD Simulations," Wind Energy, **15**, pp. 1183–1196.
[40] Jonkman, J., Butterfield, S., Musial, W., and Scott, G., 2009, "Definition of a 5-MW Reference Wind Turbine for Offshore System Development," National Renewable Energy Laboratory, Golden, CO, Report No. NREL/TP-500-38060.
[41] Schrenk, O., 1940, "A Simple Approximation Method for Obtaining the Spanwise Lift Distribution," NACA TM No. 948.
[42] Hand, M. M., Simms, D. A., Fingersh, L. J., Jager, D. W., Cotrell, J. R., Schreck, S., and Larwood, S. M., 2001, "Unsteady Aerodynamics Experiment Phase VI: Wind Tunnel Test Configurations and Available Data Campaigns," National Renewable Energy Laboratory, Golden, CO, Report No. NREL/TP-500-29955.
[43] Issa, R. I., 1985, "Solution of the Implicitly Discretized Fluid Flow Equations by Operator-Splitting," J. Comput. Phys., **62**, pp. 40–65.
[44] Rhie, C. M., and Chow W. L., 1983, "Numerical Study of the Turbulent Flow Past an Airfoil With Trailing Edge Separation," AIAA J., **21**(11), pp. 1525–1532.
[45] Smagorinsky, J., 1963, "General Circulation Experiments With the Primitive Equations," Mon. Weather Rev., **91**, pp. 99–164.
[46] Wesseling, P., 2001, "Elements of Computational Fluid Dynamics," Lecture Notes WI 4011, TU Delft, Delft, Netherlands.
[47] Schmitz, S., 2012, "XTURB-PSU: A Wind Turbine Design and Analysis Tool," http://www.aero.psu.edu/Faculty_Staff/schmitz/XTurb/XTurb.html
[48] Jha, P. K., Brillembourg, D., and Schmitz, S., 2012, "Wind Turbines Under Atmospheric Icing Conditions—Ice Accretion Modeling, Aerodynamics, and Control Strategies for Mitigating Performance Degradation," AIAA Paper No. 2012-1287.
[49] Moriarty, P. J., and Hansen, A. C., 2005, "AeroDyn Theory Manual," National Renewable Energy Laboratory, Golden, CO, Report No. NREL/TP-500-36881, http://www.nrel.gov/docs/fy05osti/36881.pdf
[50] Chattot, J. J., 2002, "Design and Analysis of Wind Turbines Using Helicoidal Vortex Model," Comput. Fluid Dyn. J., **11**(1), pp. 50–54.
[51] Du, Z., and Selig, M. S., 1998, "A 3D Stall-Delay Model for Horizontal Axis Wind Turbine Performance Prediction," 36th AIAA Aerospace Sciences Meeting and Exhibit, ASME Wind Energy Symposium, Reno, NV, January 12–15, AIAA Paper No. 98-0021.
[52] Hansen, C., 2005, AirfoilPrep, NWTC Design Code, Ver. 2.0, National Renewable Energy Laboratory, Golden, CO, last modified March 9, 2010 and retrieved on Dec. 7, 2012, http://wind.nrel.gov/designcodes/preprocessors/airfoilprep/
[53] Schmitz, S., and Chattot, J. J., 2005, "A Parallelized Couple Navier–Stokes/Vortex-Panel Solver," ASME J. Sol. Energy Eng., **127**(4), pp. 475–487.